Nano-channel-based physical and chemical synergic regulation for dendrite-free lithium plating

Qiang Guo[1,2], Wei Deng[1], Shengjie Xia[1], Zibo Zhang[1], Fei Zhao[1], Binjie Hu[2], Sasa Zhang[1], Xufeng Zhou[1] (✉), George Zheng Chen[3] (✉), and Zhaoping Liu[1] (✉)

[1] Key Laboratory of Graphene Technologies and Applications of Zhejiang Province and Advanced Li-ion Battery Engineering Laboratory of Zhejiang Province, Ningbo Institute of Materials Technology and Engineering, Chinese Academy of Sciences (CAS), Ningbo 315201, China
[2] Department of Chemical and Environmental Engineering, Faculty of Science and Engineering, University of Nottingham, Ningbo 315100, China
[3] Department of Chemical and Environmental Engineering, Faculty of Engineering, University of Nottingham, Nottingham NG7 2RD, UK

ABSTRACT

Uncontrollable dendrite growth resulting from the non-uniform lithium ion (Li$^+$) flux and volume expansion in lithium metal (Li) negative electrode leads to rapid performance degradation and serious safety problems of lithium metal batteries. Although N-containing functional groups in carbon materials are reported to be effective to homogenize the Li$^+$ flux, the effective interaction distance between lithium ions and N-containing groups should be relatively small (down to nanometer scale) according to the Debye length law. Thus, it is necessary to carefully design the microstructure of N-containing carbon materials to make the most of their roles in regulating the Li$^+$ flux. In this work, porous carbon nitride microspheres (PCNMs) with abundant nanopores have been synthesized and utilized to fabricate a uniform lithiophilic coating layer having hybrid pores of both the nano- and micrometer scales on the Cu/Li foil. Physically, the three-dimensional (3D) porous framework is favorable for absorbing volume changes and guiding Li growth. Chemically, this coating layer can render a suitable interaction distance to effectively homogenize the Li$^+$ flux and contribute to establishing a robust and stable solid electrolyte interphase (SEI) layer with Li–F, Li–N, and Li–O-rich contents based on the Debye length law. Such a physical-chemical synergic regulation strategy using PCNMs can lead to dendrite-free Li plating, resulting in a low nucleation overpotential and stable Li plating/stripping cycling performance in both the Li‖Cu and the Li‖Li symmetric cells. Meanwhile, a full cell using the PCNM coated Li foil negative electrode and a LiFePO$_4$ positive electrode has delivered a high capacity retention of ~ 80% after more than 200 cycles at 1 C and achieved a remarkable rate capability. The pouch cell fabricated by pairing the PCNM coated Li foil negative electrode with a NCM 811 positive electrode has retained ~ 73% of the initial capacity after 150 cycles at 0.2 C.

KEYWORDS

carbon nitride, Debye length, lithiophilic coating, porous structure, Li negative electrode

1   Introduction

With increasing popularity in portable electronic devices and electric vehicles, traditional lithium ion (Li$^+$) batteries are facing challenges of growing demands for higher energy density [1]. Instead, lithium metal (Li) has been widely denoted as the most promising negative electrode material and received extensive research attentions owing to its low density (0.53 g·cm^{-3}), negative redox potential (−3.04 V vs. the standard hydrogen electrode) and high theoretical specific capacity (3,860 mAh·g^{-1}) [2–4]. Meanwhile, Li negative electrode is widely regarded as a crucial part of the development of the next-generation energy storage system such as Li–air or Li–S batteries [5].

Nevertheless, the practical application of lithium metal rechargeable battery (LMRB) has been impeded mainly by physical/chemical problems of the Li negative electrode during charging/discharging. Infinite volume expansion of the Li negative electrode is a non-negligible issue, which is much more severe than graphite (≈ 10%) and silicon (≈ 400%) negative electrode materials [6, 7]. Meanwhile, Li tends to deposit in dendritic morphology in completely open space without any physical constraint [8]. Such arbitrary growth of Li can increase the porosity of the electrode and enlarge the contact area between Li and electrolyte, leading to rising inescapable side-effect. Moreover, locally concentrated Li$^+$ flux can be easily caused by inhomogeneous morphology or chemistry of the solid electrolyte interphase (SEI) layer or surface defects on the current collector at the electrode/electrolyte interface. Consequently, uneven Li$^+$ flux induces preferential growth of Li on the tips or protrusions, hence amplifying serious dendritic growth of Li. The above issues can mutually affect each other, ultimately resulting in continuous electrolyte consumption and low Coulombic efficiency (CE) as well as sharp capacity degradation of LMRBs.

Over the past decades, tremendous efforts have been devoted to tackling above-mentioned problems. Researchers have developed different strategies, including constructing artificial protective SEI layers [9–14], electrolytes optimization (e.g., adding

Address correspondence to Xufeng Zhou, zhouxf@nimte.ac.cn; George Zheng Chen, george.chen@nottingham.ac.uk; Zhaoping Liu, liuzp@nimte.ac.cn

functional salts [15–17]) and current collector modification [18–24] to achieve confined growth of Li or reduce parasitic reactions. Recently, three-dimensional (3D) scaffold decoration on Li negative electrode was reported as a viable alternative to physically guide confined growth of Li and efficiently suppress the volume expansion [8, 13, 21, 25, 26]. In addition, depending on its non-conducting or weak-conducting property, 3D scaffolds could easily avoid top deposition manner that usually occurs in traditional 3D current collectors. Meanwhile, scaffolds with abundant polar functional groups were confirmed to be able to chemically regulate Li$^+$ diffusion toward uniform Li deposition [21, 25].

Nitrogen doping of carbon materials is a typical way to provide polar functional groups (e.g., pyridinic nitrogen and pyrrolic nitrogen) for 3D scaffolds, which can interact strongly with lithium ions and enhance the lithiophilicity to alleviate inhomogeneous Li$^+$ flux [27]. For example, N-doped graphene [28] and polyacrylonitrile (PAN) nanofibers [8] were reported to be able to form strong interaction toward lithium ions, giving rise to homogeneous Li$^+$ flux. It is worth noting that graphitic carbon nitride (g-C$_3$N$_4$) with an ultra-high N content up to 57 at.% was recently demonstrated to show remarkable affinity toward Li$^+$ by forming transient Li–N bonds, which could powerfully facilitate deposition kinetics at the vicinity of the negative electrodes [22, 29–32]. For instance, 3D Ni foam coated with g-C$_3$N$_4$ sheets could guide Li deposition by adjusting the interfacial micro-electric field owing to the dominant affinity of N-containing functional groups with lithium ions [3]. In addition, ultrahigh shear modulus up to ~ 21.6 GPa within g-C$_3$N$_4$ could help suppress the dendrite proliferation during cycling [33]. Therefore, Lewis acid–base interaction-induced lithiophilic property and excellent mechanical strength intrinsically endow g-C$_3$N$_4$ with promising applications in stabilizing Li deposition behavior.

However, a fundamental issue on the effective interaction distance between Li$^+$ ions and N-containing functional groups has not yet been fully resolved in past and ongoing studies [8, 21]. It is well known that the Li$^+$ fluid behavior in 3D scaffolds is significantly determined by the size of fluid channel. In macroscopic fluids, because of the large size in fluid channel, the role of the electric double layer (EDL) is often neglected. However, when the fluid channel size further shrinks to the nanometer scale, the EDL performs an important role in regulating Li$^+$ flux [25]. Meanwhile, based on the Debye length law as shown in Eq. (1) [34], large pores can hardly provide rational space to launch efficient interaction between electronegative atoms and lithium ions.

$$L_D = \left(\frac{\sum_i n_{\infty i} e^2 z_i^2}{\varepsilon_{rs}\varepsilon_0 kT} \right)^{-\frac{1}{2}} \tag{1}$$

where L_D is the Debye length, $n_{\infty i}$ the ionic concentration, e the electron charge (1.6×10^{-19} C), z_i the ion valence, ε_{rs} the dielectric constant of solution, ε_0 the dielectric constant of vacuum (8.85×10^{-12} F/m), k the Boltzmann constant (1.38×10^{-23} J/K), and T the temperature. The Debye length reflects an important characteristic of charge shielding effect. In our system, N element in porous carbon nitride microsphere (PCNM) is regarded as an electron-rich element (Lewis-base), while Li$^+$ is positively charged (Lewis-acid). Due to the law of Lewis-base and Lewis-acid interaction, N-containing groups are always surrounded by Li$^+$, but their electric field can only act within a certain distance. Accordingly, the Debye length that reflects the range of electrostatic forces to interact with

lithium ions in electrolyte is possibly distributed at the nanometer scale. Beyond this distance, N-containing groups will basically be shielded from the electrical field of the surrounding opposite particles. Only when the distance between N-containing groups and Li$^+$ is less than the Debye length, is there indeed effective interaction between them. Thus, channel widths in a 3D scaffold should be limited to the nanometer scale in order to effectively regulate Li$^+$ flux.

Based on the concept of Debye length and excellent lithiophilic property of g-C$_3$N$_4$, we have developed PCNMs which contain abundant nanometer pores as structure units of a 3D scaffold. When coating PCNMs on Cu or Li foils, the nano-pores inside PCNMs can effectively homogenize the Li$^+$ distribution to promote homogeneous Li$^+$ deposition and construct a robust SEI through the chemical interaction between Li$^+$ and g-C$_3$N$_4$, while the interparticle micro-pores can provide enough space to accommodate and guide Li growth and relieve volume expansion in a physical way. This physical and chemical synergic regulation strategy contributes to improved Li deposition/ dissolution, resulting in stable cycling performance of the lithium metal cells.

2 Experimental section

2.1 Materials synthesis

Synthesis of bulk graphitic carbon nitride (BCN) powder. 10 g of melamine (Aladdin, Pur. ≥ 99.0%) was placed in a covered crucible. The crucible was heated at a rate of 2 °C·min^{-1} to 550 °C and held at 550 °C in argon atmosphere for 4 h. Stiff yellow g-C$_3$N$_4$ monolith was acquired after cooling to room temperature, which was then ground in a mortar to form g-C$_3$N$_4$ powders.

Synthesis of sheet carbon nitride (SCN). 5 g of melamine was dispersed in 30 mL of deionized water under continuous stirring for 30 min. Then the mixture was transferred into a 70 mL Teflon-lined stainless steel autoclave and heated at 200 °C for 12 h. After cooling, the precipitates were centrifuged and washed repeatedly with deionized water and ethanol, and dried at 80 °C for 12 h, followed by calcination in a covered crucible at 550 °C for 4 h with a heating rate of 2 °C·min^{-1} under argon to obtain yellow g-C$_3$N$_4$ nanosheets.

Synthesis of PCNMs [35, 36]. 7.92 mmol of melamine was dissolved in 40 mL of dimethyl sulfoxide (DMSO) (Aladdin, Pur. ≥ 99.0%), and equimolar cyanuric acid (Aladdin, Pur. ≥ 99.0%) was dissolved in 20 mL of DMSO. The two solutions were separately heated to 60 °C and then mixed together by stirring for 15 min. The mixture was filtered, washed 2 times with ethanol and deionized water, respectively, and then dried at 80 °C. Finally, the white powders were calcined at 550 °C for 4 h with a heating rate of 2 °C·min^{-1} under argon to obtain yellow g-C$_3$N$_4$ powders.

2.2 Electrodes preparation

Fabrication of Cu@BCN, Cu@SCN, and Cu@PCNM. The as-prepared BCN, SCN, and PCNM powders were each mixed with polyvinylidene fluoride (PVDF) in N-methyl-2-pyrrolidone (NMP, solvent) with a 1:1 mass ratio of BCN, SCN, or PCNM to PVDF. After stirring for 10 h, the slurry with a thickness of 200 μm was cast on a Cu foil and vacuum-dried at 80 °C for 6 h. The total loading density on Cu foil was ~ 1 mg·cm^{-2}. The as-obtained Cu@BCN, Cu@SCN, and Cu@PCNM were each punched into a disk of 14 mm in diameter as the working electrode.

Fabrication of Li foil@PCNM. The slurry used for preparing Cu@PCNM was cast on a 100 μm thick Li foil and vacuum-dried at 80 °C for 6 h. The as-obtained Li foil@PCNM was punched into 14 mm circular or 47 mm × 57 mm rectangular discs, respectively, as the negative electrode.

Fabrication of LiFePO$_4$ (LFP) and LiNi$_{0.8}$Co$_{0.1}$Mn$_{0.1}$O$_2$ positive electrodes. LiFePO$_4$ slurry was prepared by mixing LFP powders (Shenzhen BTR New Energy Materials Inc.), Super P, and PVDF in NMP in a mass ratio of 8:1:1, and coated on Al foil. The as-obtained LFP electrode was punched into disks with a diameter of 14 mm as the positive electrode. The areal capacity of the LFP positive electrode was ~ 2 mAh·cm^{-2}. LiNi$_{0.8}$Co$_{0.1}$Mn$_{0.1}$O$_2$ (NCM 811) (Ningbo Ronbay Lithium Battery Material Co., Ltd.) slurry was prepared by mixing Ni-rich oxides, Super P, single walled carbon nanotubes (SWCNTs), multi-walled carbon nanotubes (CNTs), and PVDF in NMP with a weight ratio of 97.80:0.40:0.02:0.28:1.50, and coated on Al foil. The as-obtained NCM 811 electrode was tailored in 43 mm × 53 mm as the positive electrode in pouch cells. The areal capacity of the NCM 811 positive electrode was ~ 3.75 mAh·cm^{-2}.

2.3 Electrochemical measurements

Two-electrode coin half cells (Li vs. Cu@BCN, Cu@SCN, and Cu@PCNM, or Li foil@PCNM vs. Li foil@PCNM). Standard CR2032 coin-type cells were assembled in an Ar-filled glove box with O$_2$ and H$_2$O content below 1 ppm. For the Li‖Cu coin half cell, 0.5 mm thick Li disc of 16.0 mm in diameter was employed as both the counter and reference electrode. The as-prepared 14 mm discs of Cu@BCN, Cu@SCN, and Cu@PCNM were employed as the working electrode. The Celgard 2500 polypropylene membrane was used as the separator (25 μm). 1 M lithium bis(trifluoromethanesulphonyl)imide (LiTFSI) in 1,3-dioxolane (DOL)/dimethoxyethane (DME) (v/v = 1:1) with 2.0 wt.% LiNO$_3$ additive was employed as the electrolyte in each cell. Electrolyte of 75 μL was added in coin cells. The galvanostatic performances were conducted at 25 °C using the Land CT 2100A system (Jinnuo Wuhan Corp, China). Li was plated galvanostatically with capacities of from 1 to 10 mAh·cm^{-2} on the Cu@BCN, Cu@SCN, and Cu@PCNM or Li foil@PCNM and then stripped galvanostatically by a cut-off potential of 0.5 V vs. Li/Li$^+$ at different current densities. Cyclic voltammetry (CV) and electrochemical impedance spectroscopy (EIS) were measured by electrochemical workstation (Solartron 1470E) using CR2032-type coin cells. The frequency range was chosen between 1 MHz and 0.01 Hz. For Li‖Li symmetrical coin cells, two identical 14 mm discs of Li foil@PCNM were assembled into symmetrical coin cells with polypropylene (Celgard 2500) as the separator.

Two-electrode coin full cells (LFP vs. Li foil@PCNM). The as-prepared 14 mm discs of Li foil@PCNM and LFP were employed as the negative and positive electrodes, respectively. The areal loading of the LFP positive electrode was 12 mg·cm^{-2}, corresponding to an areal capacity of ~ 2 mAh·cm^{-2}. Areal loading of the Li foil@PCNM negative electrode was 20 mAh·cm^{-2}. Celgard 2500 was used as the separator (25 μm). The electrolyte used herein was 1 M lithium hexafluorophosphate (LiPF$_6$) in a mixed solution of ethylene carbonate (EC) and dimethyl carbonate (DMC) (volume ratio of 3:7). Electrolyte injection was fixed at 75 μL in each coin cell. All coin cells were shelved for 8 h before testing. The LFP-based full cells were galvanostatically charged up to 4 V and then galvanostatically discharged to 2.0 V at various rates from 0.5 to 2 C. Cycling performances of the cells were tested by charging at 0.5 C and discharging at 1 C within the voltage range from 2 to 4 V.

Pouch cells (NCM 811 vs. Li foil@PCNM). As-prepared Li foil@PCNM with a size of 47 mm × 57 mm was employed as the negative electrode (20 mAh·cm^{-2}). As-prepared NCM 811 electrodes with a size of 43 mm × 53 mm was applied as the positive electrode. Single side areal loading of the positive electrode was ~ 20 mg·cm^{-2}, corresponding to areal capacity of ~ 3.75 mAh·cm^{-2}. Celgard 2500 was used as the separator (25 μm). The electrolyte with 1 M LiPF$_6$ in EC/DMC = 1:1 by volume with 2 wt.% fluoroethylene carbonate (FEC) was used (6 g·Ah^{-1}). After injecting the electrolyte, full cells were at least stored for two days to achieve full infiltration of electrolytes into pores of separators and positive electrodes. The NCM 811-based pouch cells were galvanostatically charged up to 4.3 V and then galvanostatically discharged to 2.6 V at 0.2 C. N/P ratio was around 5. Pouch cells were subjected to 100 kPa pressure during charging/discharging.

2.4 Sample characterization

The microstructure of samples were recorded by a Hitachi S-4800 field emission scanning electron microscope (SEM). X-ray diffraction (XRD) patterns were performed by using an AXS D8 Advance diffractometer (Cu Kα radiation; receiving slit, 0.2 mm; scintillation counter; 40 mA, 40 kV) from Bruker Inc. The Fourier transform infrared (FT-IR) spectrophotometer (Thermo-Fisher, Nicolet 6700) was used to characterize the chemical structure. The measurements of X-ray photoelectron spectroscopy (XPS) (Axis Ultra DLD) were conducted using Al Kα monochromatic beam (1,486.6 eV) and C 1s peak (284.8 eV) to calibrate. High-resolution transmission electron microscope (TEM) images were obtained by TEM (FEI Tecnai F20) operating at 200 kV. The Li‖Cu coin half cell in a sealed quartz cuvette was measured for the *in situ* Raman analysis. The Renishaw in Via Reflex micro-Raman was equipped with an exciting laser of 785 nm. Focused ion beam (FIB) (Helios-G4-CX) was carried out to reveal clearly the intrinsic cross-section view of samples. Surface tension/dynamic contact angle (DCAT21) was measured to show electrolyte wettability toward the samples. N$_2$ adsorption–desorption measurements (Micrometritics ASAP 2020 analyzer) were conducted at 77 K.

2.5 Ionic conductivity test

The as-prepared BCN, SCN or PCNM powders were mixed with PVDF and LiTFSI in NMP (as solvent) with the 1:1:1 mass ratio of BCN, SCN or PCNM to PVDF to LiTFSI. After stirring for 10 h, the slurry with a thickness of 200 μm was cast on a Cu foil and vacuum-dried at 80 °C for 6 h. The as-obtained BCN, SCN or PCNM and LiTFSI@Cu were punched into disks with a diameter of 19 mm as the working electrode. The steel disc with a diameter of 14 mm was used as the counter electrode. The EIS of cell was tested at various temperatures. The ionic conductivity was calculated by Eq. (2)

$$\sigma = \frac{L}{R \cdot S} \tag{2}$$

where σ stands for ionic conductivity, L is the solid-state electrolyte thickness, R the resistance, and S the contact area of steel disc.

3 Results and discussion

3.1 Materials characteristics

Porous g-C$_3$N$_4$ microspheres were synthesized by thermal poly-condensation of supramolecular aggregates of melamine and cyanuric acid according to the previous work by Liu et al. [37].

SEM image (Fig. 1(a)) illustrates that each g-C$_3$N$_4$ microsphere has porous and flower-like morphology with a typical diameter of ~ 3.5 μm. Two-dimensional (2D) g-C$_3$N$_4$ nanosheets with an average thickness of ~ 40 nm aggregate randomly in the microspheres to form porous structure with nanometer scale pore sizes. It is predicted that the 3D geometry made up of 2D nanosheets is more robust than individual 2D g-C$_3$N$_4$ nanosheets. Also, as demonstrated in the TEM image (Fig. 1(b)), porous 3D architecture assembled by 2D g-C$_3$N$_4$ nanosheets has higher surface area and more voids than BCN owing to the bendable and random layout of 2D nanosheet units (Figs. S1(a) and S1(b) in the Electronic Supplementary Material (ESM)). This porous property is beneficial for electrolyte penetration and adsorption and provides more space for Li deposition. As depicted in Fig. S2 in the ESM, it is further verified by evident volume difference between BCN and PCNM with the same weight.

XPS analysis was performed to determine the surface chemical composition and electronic states of PCNM, and the results are shown in Fig. S3 in the ESM and Fig. 1(c). Two peaks centered at 284.9 and 287.4 eV can be found in the C 1s spectrum of PCNM (Fig. S3 in the ESM), which are assigned to graphitic carbon (C–C) in g-C$_3$N$_4$ and sp^2-hybridized carbon (N=C–N) [38] in the aromatic ring attached to the –NH$_2$ or –NH group [38, 39], respectively. The high-resolution spectrum of porous microspheres also displays remarkable N 1s signals which can be deconvoluted into four peaks at 399.0, 400.0,

401.2 and 404.4 eV, corresponding to sp^2-nitrogen in triazine ring (C=N–C) [40], tertiary N bonded to C atoms in form of N–(C)$_3$ or H–N–(C)$_2$ [41], terminal amino groups (C–NH$_x$) [42] and heterocycles, respectively. These results further confirm the existence of abundant N element as Lewis-base sites in PCNM. Meanwhile, the atomic percentage of C (46.63%) and N (53.37%) measured by TEM (Table S1 in the ESM) is also in good agreement with the XPS results.

For comparison, two other g-C$_3$N$_4$ samples of BCN and SCN with different morphologies were also synthesized according to the method provided in the experimental section, whose morphology and physical properties are presented in Figs. 1(d)–1(f) and Fig. S4 in the ESM. It is found that SCN exhibits typical laminar morphology as displayed in the SEM and TEM images (Figs. S4(a) and S4(b) in the ESM), similar as graphene. It has a lateral size of several microns and a thickness of tens of nanometers. The as-prepared BCN sample shows typical particle morphology with irregular shapes and size ranging from several to a few dozen microns (Fig. S4(c) in the ESM). Solid internal structure of BCN particles can be discerned by TEM (Fig. S4(d) in the ESM), which is totally different from the porous structure of PCNM.

Typical XRD patterns of BCN, SCN and PCNM samples are displayed in Fig. 1(d). All three samples have two characteristic peaks at 13.2° (d = 0.675 nm) and 27.5° (d = 0.325 nm), corresponding to the diffraction of the (100) (inter-planar stacking) and (002) (in-planar structural packing motif) crystal
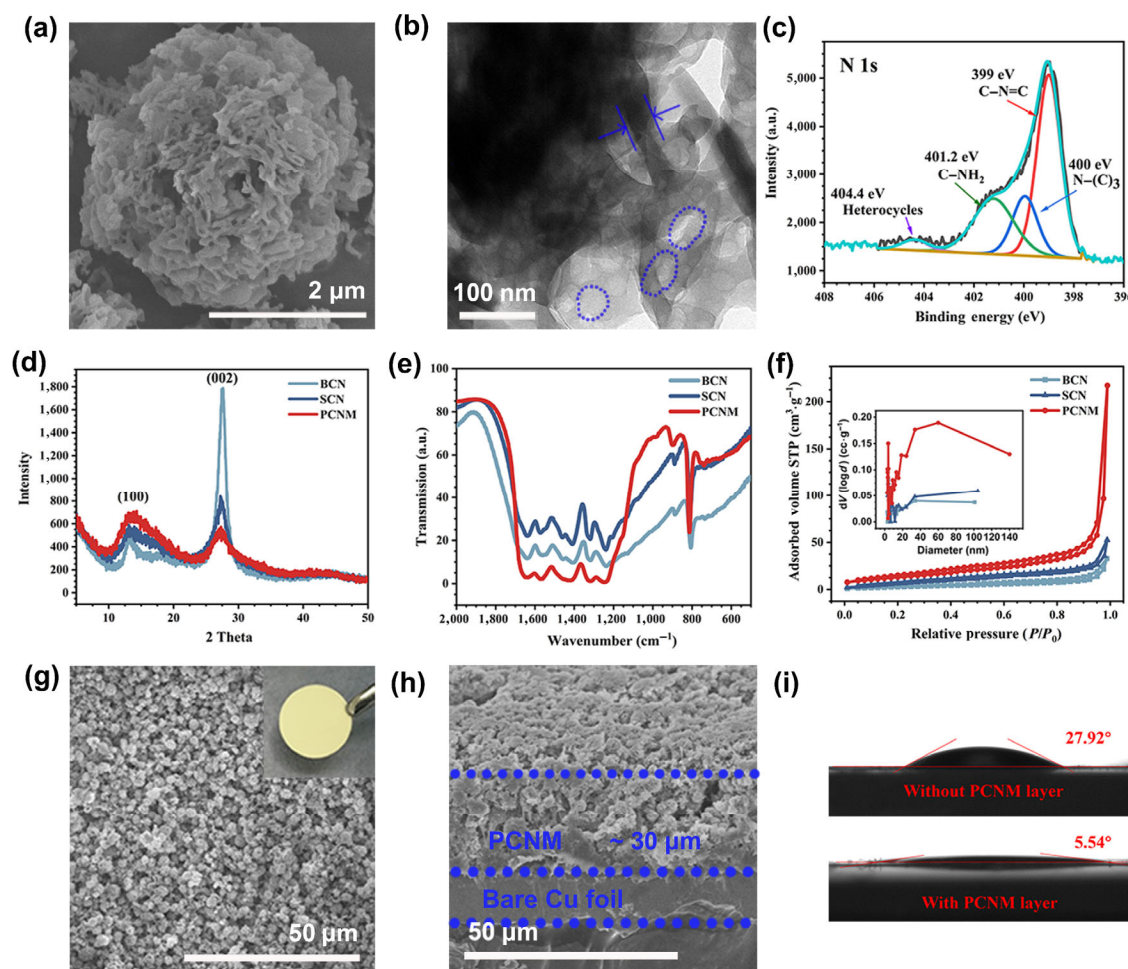

Figure 1 Microstructure and physical properties of g-C$_3$N$_4$ materials. (a) SEM image and (b) TEM image of PCNM. (c) N 1s XPS spectra of PCNM. (d) XRD patterns, (e) FT-IR spectra, and (f) nitrogen adsorption and desorption isotherms of BCN (black line), SCN (blue line) and PCNM (red line). The inset of (f) shows the pore size distribution data. (g) Top-view and (h) cross-section view SEM images of Cu@PCNM. The inset of (g) shows the optical photograph of Cu@PCNM. (i) Contact angles of electrolyte toward Cu foil coated with and without PCNM.

plane of g-C₃N₄, respectively [43–45]. The diffraction peaks of PCNM have the largest full width at half maxima comparing with those of BCN and SCN, suggesting the smallest crystal size of g-C₃N₄ in PCNM. Based on Debye–Scherrer equation, the crystal size of g-C₃N₄ in PCNM along the (002) crystal plane is calculated to be ~ 35 nm, which is in good agreement with the thickness of the g-C₃N₄ nanosheets in this sample as shown in the TEM image (Fig. 1(b)). The interplanar spacing calculated from the XRD patterns is also in accordance with the selected area electron diffraction (SAED) rings presented in Fig. S5 in the ESM.

The FT-IR spectra for all synthesized samples are depicted in Fig. 1(e). All g-C₃N₄ samples show almost identical peaks shape in the range of 1,200–1,650 cm^{-1}, which corresponds to the typical stretching vibration of aromatic rings in carbon nitride. The peak at ~ 1,662 cm^{-1} is assigned to the stretching vibration of C–N. The peaks at 1,216, 1,310, and 1,405 cm^{-1} belong to the stretching vibration of C–N in aromatic hydrocarbons, and the peak appearing at 807 cm^{-1} corresponds to the combined vibration of triazine unit [46–48]. All these peaks confirm the successful synthesis of g-C₃N₄ in combination with XRD and XPS results.

To further understand the pore structure over different g-C₃N₄ materials which is important in Li⁺ regulation, detailed pore structure was characterized by nitrogen adsorption and desorption isotherms (Fig. 1(f)). It is found that the adsorption quantity increases linearly with rising relative pressure to 0.8 and then increases exponentially to atmospheric pressure, which suggests that a broad range of pores have been formed. Compared to SCN and BCN, hysteresis between the adsorption and desorption branches in the exponentially increased section can be observed obviously in PCNM, suggesting it possesses a more mesoporous structure. The type of hysteresis loop of PCNM is probably assigned to H3 (IUPAC) which elucidates the presence of wedge-shaped pores resulting from loosely packed nanosheets. Pore size distribution data (inset in Fig. 1(f)) using Barrett–Joyner–Halenda (BJH) model also further proves the fact that PCNM possesses a broad pore size distribution ranging from 2 to 140 nm. In particular, pores size of between 40 and 80 nm are dominant in PCNM, which is in good agreement with the size of nanopores observed in the TEM image (Fig 1(b)). PCNM also possesses the largest Brunauer–Emmett–Teller (BET) specific surface area (49.3 $m^2 \cdot g^{-1}$), pore volume (~ 0.3 $cc \cdot g^{-1}$) and average pore size (~ 27.3 nm) among three g-C₃N₄ samples (Table S2 in the ESM), which is contributed by its unique morphology. The abundant nano-sized pores (< 150 nm) in PCNM endow suitable space to effectively develop the uniformity of Li⁺ flux based on the Debye length law. It is worth noting that the apparent shift of the decomposition temperature of PCNM toward a lower region compared to BCN and SCN (Fig. S6 in the ESM) also reveals the rich porous structure in PCNM, which enables to enhance gas permeation and facilitate heat transfer.

The as-prepared PCNM powders were mixed with PVDF in NMP solvent to form a slurry which was subsequently cast on a Cu foil to form a coating layer of 3D scaffold. Light yellow coating can be observed in the inset image of Fig. 1(g). As demonstrated in Figs. 1(g) and 1(h), the coating with the thickness of ~ 30 μm displays a relatively smooth surface. Random packing of PCNM particles in this coating layer forms inter-particle pores (Fig. S7 in the ESM), along with internal nanopores inside each g-C₃N₄ microsphere. Uniform distribution of N, and C as well as F (from PVDF) elements over the entire coating layer are found via energy dispersive spectroscopy (EDS) mapping as presented in Fig. S8 in the ESM. Following

the same preparation process, SCN with sheet-like morphology forms a flat coating layer with a much lower thickness of ~ 5 μm than that of PCNM (Figs. S9(a) and S9(b) in the ESM). In contrast, a rough surface with larger pores is formed in the BCN coating layer (Figs. S9(c) and S9(d) in the ESM), owing to the large particle size of BCN structure units. The morphology of coating layers using three different g-C₃N₄ materials is expected to take distinct effects on the behavior of Li deposition. SCN coating layers composed of densely stacked g-C₃N₄ nanosheets cannot provide extra space to accommodate deposited Li and fail to release stress originated from Li dendrites in spite of the presence of abundant nitrogen-containing functional groups. So Li dendrites still cannot be physically alleviated in the case of SCN coating. The large particle size of BCN brings about relatively large cavities in the coating layer, which may hardly work in chemically homogenizing according to the Debye length law. It is believed that PCNM coating can provide enough space to accommodate/guide Li growth. Besides, pristine nanoscale pores in PCNM can effectively homogenize the Li⁺ distribution. Thus, dense and flat deposition of Li can be highly expected based on such physical and chemical synergic regulation mechanism in the case of PCNM.

To understand further the interaction between the electrolyte and the PCNM coating, the wettability between these two was measured using contact angle methods. Results in Fig. 1(i) manifest that the presence of the PCNM layer results in a sharp reduction of contact angle from 27.92° to 5.54°, which suggests a marked improvement of the electrolyte wettability. While bare Cu foil and Li foil (24.7° in Fig. S10(a) in the ESM) [7] remain comparatively poor wettability with ether-based electrolytes. It is reported that the electrolyte wettability has a close relationship with the uptake amount of liquid electrolyte. Hence higher electrolyte concentration has strong impacts on the distribution of Li⁺ flux over the entire Cu/Li surface during cycling [49]. It is believed that such a superior electrolyte wettability of the PCNM layer is beneficial to obtain the uniform Li⁺ flux and relieve uneven Li⁺ transport as well as deposition. Interestingly, as shown in Figs. S10(b) and S10(c) in the ESM, PCNM layer performs stronger water-repellent than bare Cu foil, which probably prevents Li from contacting water and reduces safety risks in LMRBs when using Li foil@PCNM.

3.2 Morphology of Li plating

Figure 2 exhibits different morphologies of metallic Li plated on bare Cu foil, Cu@SCN, Cu@BCN, and Cu@PCNM electrode (Li@Cu@SCN, Li@Cu@BCN, and Li@Cu@PCNM). Notably, without lithiophilic decoration, lithium ions tend to deposit on spots where the cracks of SEI appear and tips of surface bumps emerge on the surface of bare Cu foil (Fig. 2(a)) [50]. With Li further depositing on existed Li whiskers, thick and porous dendritic morphologies are formed (Figs. 2(g) and 2(h)), leading to continuous consumption of electrolyte and an increase in irreversible Li. Due to the lack of enough space to accommodate Li growth and eliminate stress generated from Li dendrites, the SCN layer would be easily pierced and remarkable Li dendrites still can be observed on Cu@SCN (Figs. 2(b), 2(j), and 2(k)) especially at high deposition capacity i.e., 5 $mAh \cdot cm^{-2}$. More importantly, due to the absence of vertical depth of g-C₃N₄ walls in SCN coating, lithium ions cannot be affected effectively and only pass through the gaps between g-C₃N₄ nanosheets to deposit on Cu foil. Although the porous structure is formed in the BCN coating due to random stacking of g-C₃N₄ particles (Fig. 2(l) and Figs. S8(c) and S8(d) in the ESM), the Li⁺ flux cannot be efficiently affected by the
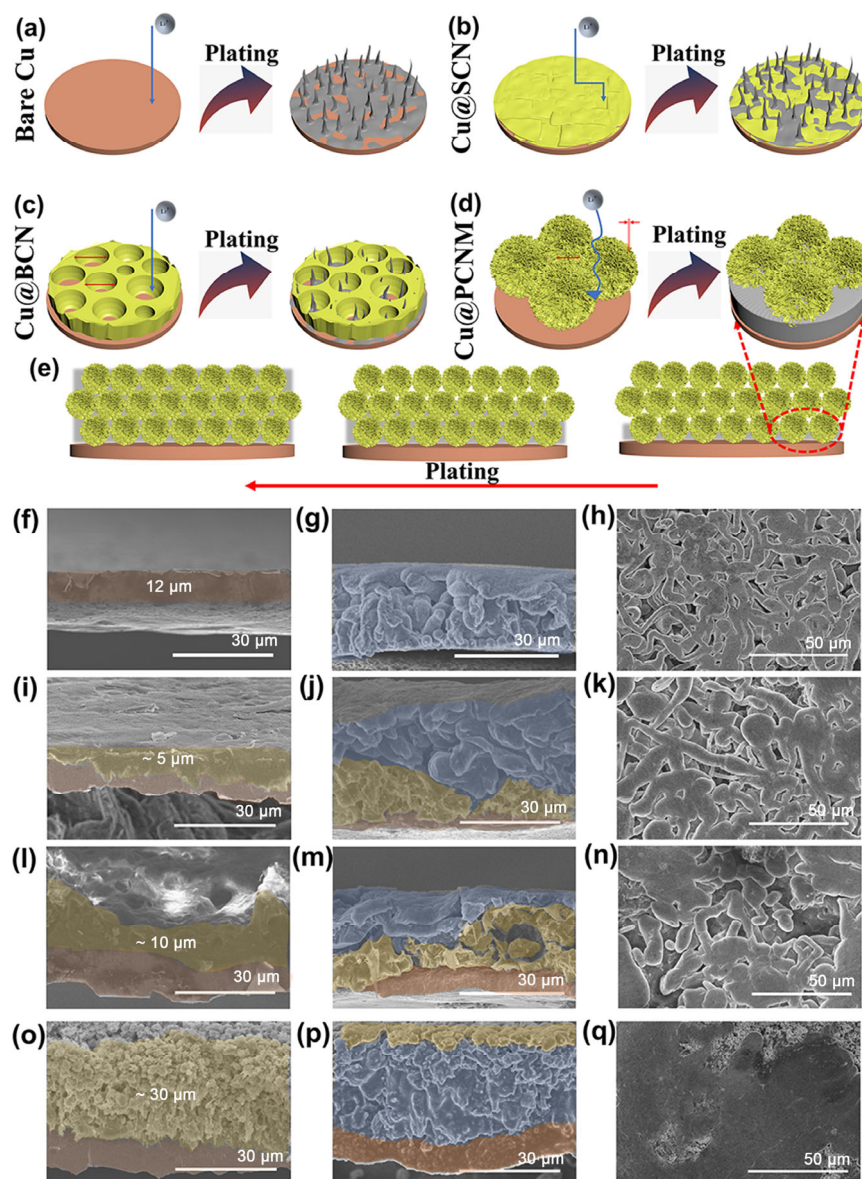
Figure 2 Diagrams showing the morphology of electrodeposited Li on (a) bare Cu foil, (b) Cu@SCN, (c) Cu@BCN, and (d) Cu@PCNM, and (e) Li plating process on Cu@PCNM. (f) SEM image of bare Cu foil. (g) Cross-section view and (h) top-view SEM images of Cu foil after plating with 5.0 mAh·cm^{-2} of Li. (i) SEM image of Cu@SCN. (j) Cross-section view and (k) top-view SEM images of Cu@SCN after plating with 5.0 mAh·cm^{-2} of Li. (l) SEM image of Cu@BCN. (m) Cross-section view and (n) top-view SEM images of Cu@BCN after plating with 5.0 mAh·cm^{-2} of Li. (o) SEM image of Cu@PCNM. (p) Cross-section view and (q) top-view SEM images of Cu@PCNM after plating with 5.0 mAh·cm^{-2} of Li. The regions marked with light blue, light red, and light yellow colors correspond to plated Li, Cu foil and g-C$_3$N$_4$ coatings, respectively. A current density of 1 mA·cm^{-2} was used for the measurement.

surface Lewis-base sites of BCN particles because of the large micrometer scale pore size (Fig. 2(c)), still leading to the formation of porous and dendritic Li (Figs. 2(m) and 2(n)). Only when there exists nanometer scale pores that tailor Li$^+$ diffusion behavior and micrometer scale pores that provide space for Li deposition at the same time, can the Li$^+$ flux be homogenized and dense and flat deposition of Li be successfully developed, which is the case that occurs on Cu@PCNM electrode (Figs. 2(d), 2(p), and 2(q)). To clearly illustrate Li deposition behavior within PCNM, morphology of the Cu@PCNM electrode at different deposition capacities (from 0.5 to 15 mAh·cm^{-2}) was characterized (Fig. S11 in the ESM). It is observed that PCNM can accommodate the maximum lithium deposition areal capacity of ~ 5 mAh·cm^{-2}. Below 5 mAh·cm^{-2}, Li tends to form a filling-like deposition within the interparticle pores (Figs. S11(b)–S11(e) in the ESM) as presented in Fig. 2(e). When the deposition areal capacity is beyond

5 mAh·cm^{-2}, the electrodeposited Li tends to continuously grow on the surface of the PCNM coating layer, while keeps a planar deposition manner. Such behavior is probably due to the enriched lithium ions at the electrode/electrolyte interface induced by abundant Lewis-base sites in PCNM. Even when the Li deposition areal capacity reaches 15 mAh·cm^{-2}, the surface of the plated Li on Cu@PCNM is still smooth. In contrast, deposited Li shows porous dendrite structure on bare Cu (Fig. S12 in the ESM). It is noteworthy that the plated metallic Li can strip from the Cu@PCNM reversibly, making the matrix recover to its pristine morphology (Figs. S12(a)–S12(d) in the ESM) and confirming its structural robustness.

3.3 SEI characterization

To clarify the specific morphology of the deposited Li, *ex situ* FIB-SEM characterization was further conducted over Cu@PCNM (Fig. 3(a)) and bare Cu (Fig. 3(b)) with plating areal

capacity of 15 mAh·cm⁻². The cross-section view of FIB-SEM image clearly reveals that the interparticle pores of PCNM coating are almost fully filled with Li (Fig. 3(a)), while partial nanopores inside g-C₃N₄ microspheres are still left. EDS mapping (Fig. S13 in the ESM) confirms that N element dominates in these porous regions, which verifies that the porous parts are g-C₃N₄ materials rather than porous Li. The above results indicate that lithium ions not only diffuse through but also partially deposit within pores assembled by g-C₃N₄ nanosheets, which demonstrates that micro/nano hybrid channels in PCNM are highly integrated with Li. These results support our claim that abundant nanopores of PCNM can facilitate synergically the formation of uniform Li⁺ flux and guide dense Li growth, which can give rise to more stable and reversible cycling behaviors. In striking contrast, the porous and dendritic structure of electrodeposited Li is generated on bare Cu foil. Besides, remarkably thick SEI wrapping on Li dendrites is due to the uneven Li⁺ deposition and electrolyte decomposition as well as the formation of by-products, resulting in poor cycling stability and a dramatic drop in CE.

In order to further understand the influence of PCNM in regulating Li plating, SEI compositions of freshly deposited Li on Cu@PCNM and bare Cu were characterized by XPS. Full spectra are presented in Fig. S14 in the ESM. In F 1s spectra, Li–F and C–F signals are observed in both electrodes, which result from the decomposition of LiTFSI salt [15]. LiF is well-known as an excellent SEI component for its high interfacial energy toward Li and high mechanical strength. Therefore,

it is efficient to suppress dendrite growth, which contributes to uniform Li deposition. Higher intensity of the Li–F signal in the case of Cu@PCNM as compared with that of bare Cu implies that N-containing Lewis-base sites in PCNM increase the concentration of TFSI anions at the deposition interface owing to their strong interaction with lithium ions, leading to robust SEI. Meanwhile, the contents of LiN_xO_y/N–SO$_x$ and Li–N (Li₃N) species on Li@Cu@PCNM are also higher than those on Li@Cu, revealing that increasing amounts of NO₃⁻/TFSI⁻ have been reduced to form the resulting SEI in the presence of PCNM. As Li₃N is a super conductor of lithium ions [51, 52], Li₃N-enriched SEI on Li@Cu@PCNM can improve Li⁺ transportation for better Li plating/stripping behavior. In addition, new emerged Li–O signal (Li₂O) on Li@Cu@PCNM verifies that decomposition of NO₃⁻ also facilitates the formation of more inorganic Li₂O grains in the SEI. Furthermore, higher content of Li₂S–O$_x$ (Li₂SO₄, Li₂SO₃ and Li₂S signals at ~ 169.5, ~ 167, and ~ 160.35 eV, respectively) resulting from electrochemical reduction of TFSI⁻ (Fig. S15 in the ESM) also further proves the PCNM-driven enhancement in cation and anion concentration, which plays an essential role in constructing robust and stable SEI. Notably, the top surface of the SEI formed in the bare Cu foil has a much stronger C–C/C–H (284.8 eV), C–O (286.3 eV) and C=O (288.eV) [53] signals compared with Li@Cu@PCNM, indicating huge electrochemical degradation of organic solvent during Li plating. In brief, an increase in inorganic composition (Li–F, Li–N and Li–O) and reduction in organic composition (C–C/C–H) verify the
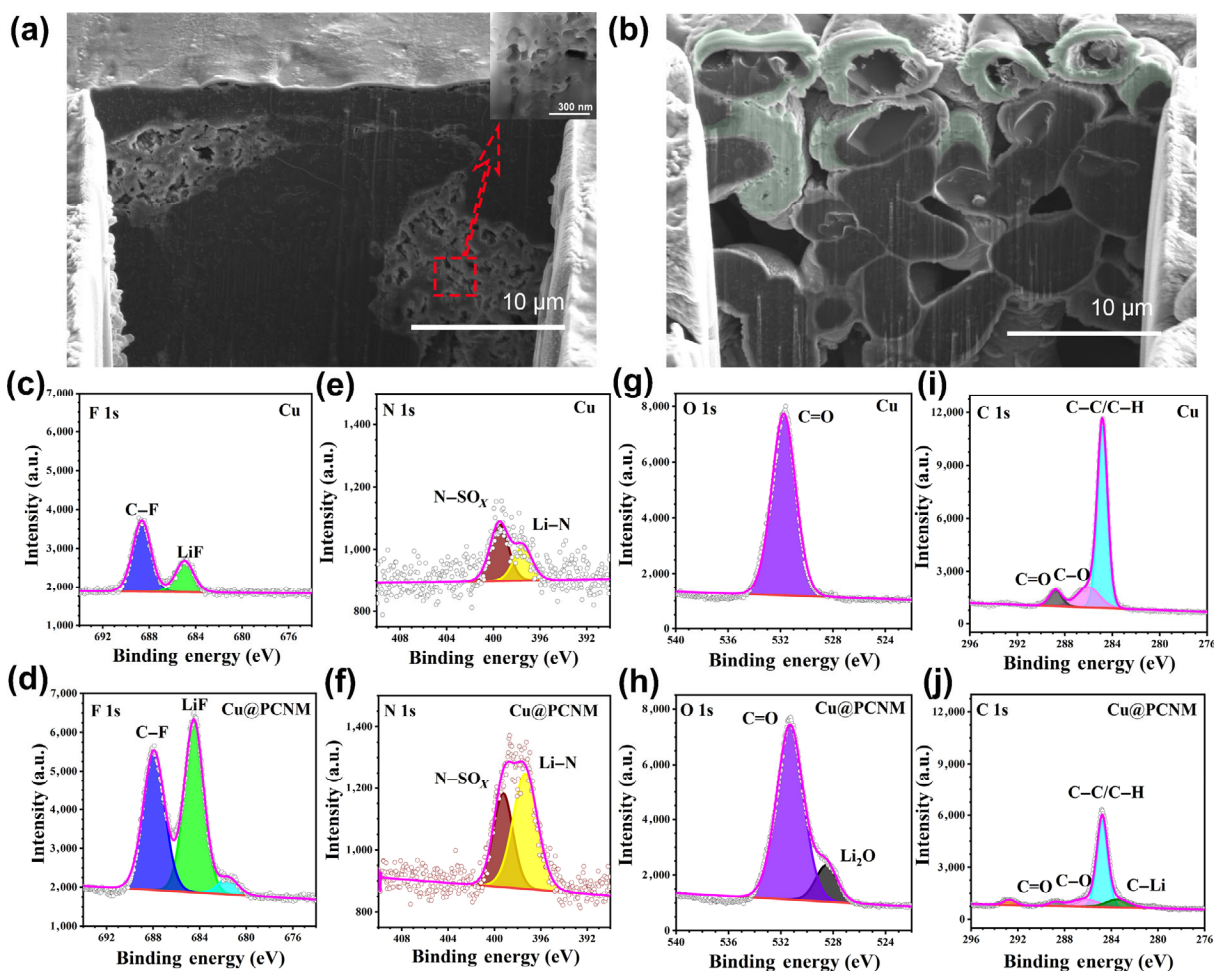

Figure 3 SEI characterization of deposited Li in bare Cu and Cu@PCNM. Cross-sectional FIB-SEM images of (a) Cu@PCNM and (b) bare Cu with plating 15 mAh·cm⁻² at 1 mA·cm⁻². ((c) and (d)) F 1s, ((e) and (f)) N 1s, ((g) and (h)) O 1s, and ((i) and (j)) C 1s XPS spectra of the surface of plated Li on Cu foil coated with ((d), (f), (h), and (j)) and without PCNM ((c), (e), (g), and (i)). Light green districts in (b) represent thick SEI layer.

formation of more robust SEI when PCNM coating is employed. It is mainly due to enriched anion distribution at the interface, which is caused by the chemical adsorption of lithium ions by Lewis-base sites in g-C_3N_4. Such robust SEI with high Li^+ conductivity can play a crucial role in dendrite-free Li plating/stripping during long cycling.

3.4 Electrochemical performances in half cells

Figures 4(a)–4(d) display the CE and long-term electrochemical stability in a half-cell configuration composed of metallic Li as the counter electrode coupled with different working electrodes (bare Cu foil, Cu@SCN, Cu@BCN, and Cu@PCNM). Among all electrodes, Cu foil exhibits the most serious fluctuation in CE and obvious overcharge behavior within 60 cycles with a high current density (2.0 mA·cm^{-2} with 1.0 mAh·cm^{-2}), which may be ascribed to the uncontrollable Li dendrite-induced electrolyte depletion and generation of by-product (Fig. 3(b)). The CE of Cu@SCN drops rapidly in the initial 20 cycles. Cu@BCN maintains comparatively stable CE with larger than 80% within 40 cycles. In comparison, the CE of the Cu@PCNM cell keeps stable for over 100 cycles. Similarly, as exhibited in Fig. 4(b), Cu@PCNM has the most stable overpotential (< 35 mV) over long-term cycling. Figure 4(c) shows the magnified voltage profiles from 0 to 2 h. Apparently, the overpotential of Cu@SCN is almost the same as that of Cu@PCNM, which is less than Cu@BCN's by ~ 30 mV, probably due to the affinity

of 2D g-C_3N_4 nanosheets in SCN with interfacial lithium ions. Bare Cu foil shows drastic voltage fluctuation and an increasing overpotential as the test time increases. Li nucleation behaviors were further explored via the voltage–capacity profiles in Fig. 4(d). Cu@PCNM exhibits the smallest nucleation overpotential of 34.59 mV. The highest and most stable CE of Cu@PCNM implies that the effective transient Li–N bonds formed due to abundant nanopores in PCNM induce stabilized and uniform Li^+ distribution near the deposition sites, which gives rise to dense deposition morphology with little dendrites and a reduced overpotential [3].

Different current densities were applied on the Li‖Cu cells using Cu@PCNM and bare Cu foil (Fig. 4(e)). It can be seen that the voltage hysteresis of Cu@PCNM only increases from ~ 30 to ~ 95 mV when the current density is increased from 0.5 to 3 mA·cm^{-2}. In contrast, Cu foil shows dramatic hysteresis change from ~ 127 to ~ 300 mV. Also, the excellent reversible property is confirmed on the Cu@PCNM electrode. The unstable voltage profile of bare Cu foil implies the formation of excessive SEI and catastrophic structural evolution, which contribute to drastic enlargement of voltage hysteresis at high current densities [54].

The CE with current density varying from 0.5 to 1 mA·cm^{-2} at 1 mAh·cm^{-2} was studied as well (Fig. S16 in the ESM). The Cu@PCNM cell achieves comparatively higher and more stable CE of > 90% at 1 mA·cm^{-2} and > 98% at 0.5 mA·cm^{-2}
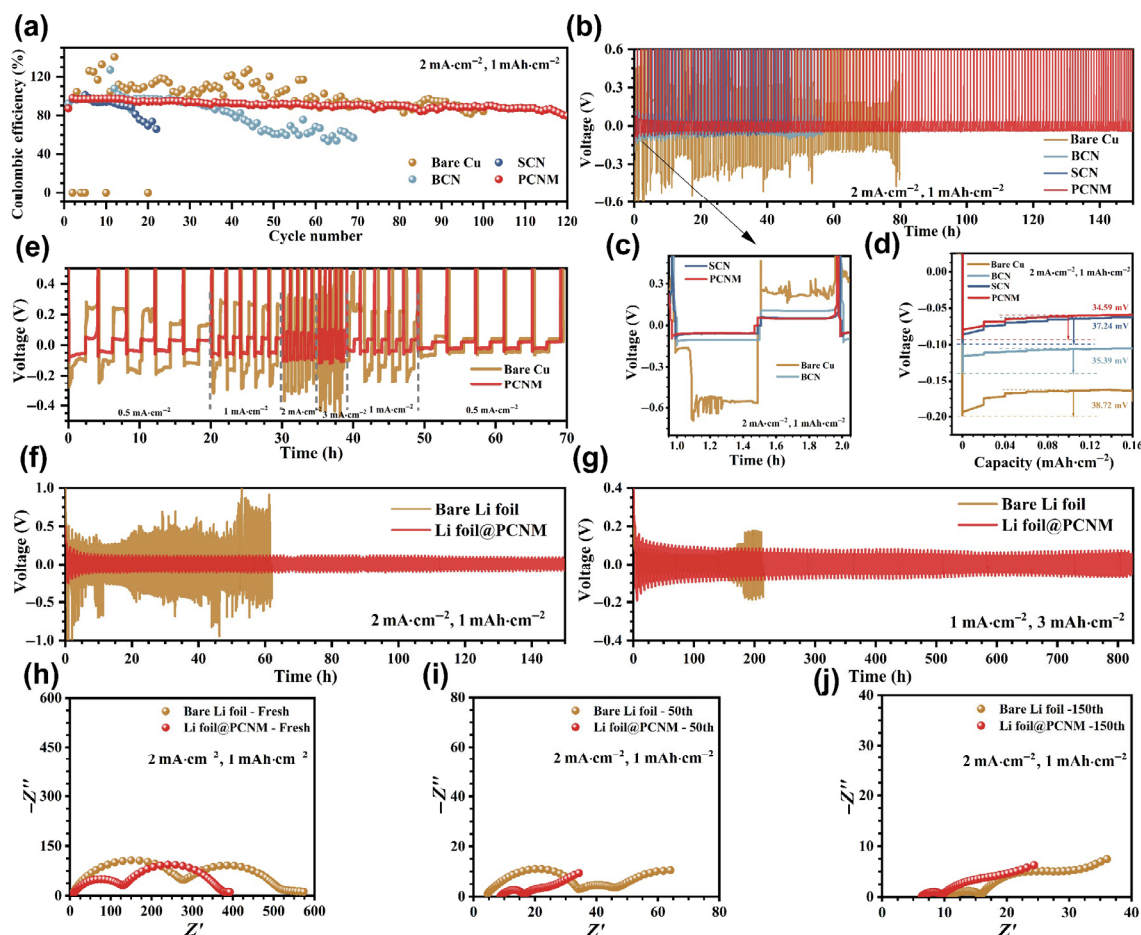

Figure 4 Electrochemical performances of Cu foil/Li foil coated with PCNM materials in Li‖Cu coin half cells and Li‖Li coin symmetrical cells. Comparison of (a) CE, (b) voltage profiles, (c) magnified voltage profiles within the plating time range of 0–2 h, and (d) nucleation overpotential of Li plating on/stripping from bare Cu foil electrode and Cu foil coated with SCN, BCN, and PCNM with an areal capacity of 1.0 mAh·cm^{-2} at 2.0 mA·cm^{-2}. (e) Comparison of voltage profiles of Li plating/stripping on Cu foil coated with and without PCNM at different current densities ranging from 0.5 to 3 mA·cm^{-2} with an areal capacity of 1 mAh·cm^{-2}. The galvanostatic plating/stripping profiles of Li‖Li symmetrical cells with an areal capacity of (f) 1.0 mAh·cm^{-2} at 2.0 mA·cm^{-2}, and (g) 3 mAh·cm^{-2} at 1 mA·cm^{-2} using Li foil@PCNM and bare Li foil electrodes. The EIS of the bare Li foil electrode and Li foil@PCNM before cycling (h), and after 50 (i) and 150 (j) cycles with an areal capacity of 1.0 mAh·cm^{-2} at 2.0 mA·cm^{-2}.

before 170 cycles. With a high areal capacity of 5 mAh·cm⁻² at 0.5 mA·cm⁻², Cu@PCNM still maintains a high CE value of 98% before 60 cycles. Even at an ultrahigh areal capacity of 10 mAh·cm⁻², the high CE (> 97%) before 30 cycles is obtained. In contrast, the CE of Cu foil becomes very unstable only after a few cycles under the above conditions. The voltage hysteresis in Fig. S17 in the ESM also reflects that the Cu@PCNM cell keeps relatively stable cycling performance with a low overpotential of less than 20 mV for more than 900 h at areal capacities of 1, 5 and 10 mAh·cm⁻², and ~ 30 mV for more than 200 cycles with an areal capacity of 1 mAh·cm⁻² at 1 mA·cm⁻².

The cycling performance of cells strongly relies on the stability of SEI on the electrode materials. Thus, the interfacial stability of the SEI was further studied by EIS (Figs. S18(a) and S18(b) in the ESM). Cu@PCNM shows a smaller semicircle than the bare Cu foil in the high-frequency range after both 50 and 150 cycles, which indicates that the SEI formed on Cu@PCNM has a smaller interface impedance and a smaller charge-transfer resistance than that on the Cu foil, and confirms that the uniform deposition of Li over Cu@PCNM facilitates the formation of a uniform SEI layer with low resistance.

Morphology of Cu@PCNM and bare Cu after 30 and 60 cycles (Figs. S19(a)–S19(h) in the ESM) with an areal capacity of 2 mAh·cm⁻² at 1.0 mA·cm⁻² was measured. Apparent dendrite-like dead Li continuously accumulates on bare Cu during plating/stripping processes, which contributes to the volume expansion (~ 16 μm after 60 cycles) and increasing internal resistance as well as huge electrolyte consumption. In comparison, the comparatively intact structure of PCNM can be maintained and the accumulation of dead lithium on the surface is not discerned even after 60 cycles, revealing the essential role that PCNM plays in suppressing the formation of Li dendrites and lowering volume changes during charging/discharging. In fact, the composition and structure of PCNM still remain stable after cycling (Fig. S20 in the ESM), which proves its long-term effectiveness in guiding uniform and reversible Li plating/stripping.

To employ PCNM in actual LMRBs, PCNM is coated on Li foil to form composite Li negative electrode. Long-term cycling stability and the stripping/plating process of symmetric cells assembled with identical Li foil@PCNM electrodes were investigated at high current densities and high capacity. As presented in Fig. 4(f), Li foil symmetric cell shows a high voltage hysteresis (~ 250 mV) in the initial stage, which is much higher than that of the Li foil@PCNM symmetric cell (~ 85 mV). As the cycling continues, the voltage hysteresis of the Li symmetric cell rapidly increases to about 500 mV accompanied with apparent voltage fluctuation appearing after 20 h, which possibly implies the failure of the cell. This may be due to the irregular growth of dendrites on the surface of the Li foil during the stripping/plating cycling. Then, Li dendrites with large surface area continuously react with the electrolyte to form the SEI and partially "dead Li", leading to growing internal resistance. In comparison, the Li foil@PCNM symmetric cell shows more stable cycling performance for more than 140 cycles, which is because of the nanopore-induced uniform Li⁺ flux and PCNM-driven confined deposition. As shown in Fig. S21 in the ESM, Li foil@PCNM symmetric cell also exhibits superior cycling performance under higher current density (1 mAh·cm⁻² at 4 mA·cm⁻²). With an increasing areal capacity to 3 mAh·cm⁻², the Li foil@PCNM cell still exhibits a low overpotential of ~ 45 mV and good cycling stability with more than 800 h. Li foil cell displays a steady overpotential (~ 45 mV) in the initial stage followed by a sudden boost after 150 cycles due to possible short circuits. The stability of SEI

interface in Li foil@PCNM and bare Li foil during cycling (1 mAh·cm⁻² at 2 mA·cm⁻²) was analyzed by EIS. Notably, Li foil@PCNM shows lower interfacial resistance (128 Ω) before cycling compared to bare Li foil (280.3 Ω). Specific resistance data derived from the fitting process is listed in Table S3 in the ESM. After 50 and 150 cycles, Li foil@PCNM still performs much smaller interfacial resistance of 4.468 and 3.046 Ω, respectively, which benefits from the fact that nanopore-driven uniform Li⁺ distribution due to effective transient Li–N bonds and intact and stable electrode structure during cycling due to interparticle pore induced low volume changes [55].

3.5 Li⁺ regulation by g-C₃N₄ materials

The difference in interaction with lithium ions of different g-C₃N₄ materials was characterized by measuring the Li⁺ conductivity (corresponding to Li⁺ transfer kinetics) of PVDF/LiTFSI-based solid-state electrolyte added with BCN, SCN, or PCNM powders (see details in the experimental section). g-C₃N₄ materials can facilitate Li⁺ transportation in PVDF matrices owing to site-to-site hopping of Li⁺ via Lewis-base sites in g-C₃N₄ [56]. g-C₃N₄ materials with different morphologies and pore structures will take different effect with lithium ions, ultimately causing different influence on ion transportation ability. It is believed that enhancement in Li⁺ conductivity is ascribed to more efficient interaction with lithium ions of g-C₃N₄. According to Fig. 5(a), ionic conductivities of solid-state electrolytes with different g-C₃N₄ materials all increase with increasing temperature from 40 to 100 °C. PCNM-based one achieves the most superior ionic conductivity compared with the other two (Table S4 in the ESM). The activation energy of g-C₃N₄ materials was calculated via temperature dependent EIS tests. Data acquired from all cases were fitted to straight lines using the following Arrhenius equation

$$\frac{T}{R_{ct}} = A \exp\left(-\frac{E_a}{RT}\right) \tag{3}$$

where E_a is the activation energy, T the absolute temperature, R the gas constant (8.314 J·(mol·K)⁻¹), R_{ct} the interfacial Li⁺ transfer resistance, and A the pre-exponential factor [57]. The activation energy upon PCNM, SCN and BCN are valued at 28.88, 30.94 and 37.30 kJ·mol⁻¹, respectively (Fig. 5(b)), which further verifies the superior role of PCNM with unique pore structure in interaction with lithium ions than that of BCN and SCN.

CV test was employed for Li plating/stripping between −0.2 and 0.5 V at scan rates from 0.2 to 10 mV·s⁻¹ to investigate the influence of Li–N interaction on the electrochemical reaction process of lithium ions. In bare Cu foil, the peak current follows the classic linear dependence with the square root of the scan rate ($v^{0.5}$), while peak current on Cu@PCNM electrode demonstrates a curved linear relationship with $v^{0.5}$, manifesting that lithium ions are under both diffusion and surface controlled process due to the interaction of PCNM with lithium ions (Fig. S22(c) in the ESM). Furthermore, the peak current and exchange current density on Cu@PCNM are much larger than that in the bare Cu foil (Figs. S22(a)–S22(d) in the ESM), which verifies that the electrochemical reduction process of lithium ions is apparently improved owing to strong Li–N interaction.

Raman spectroscopy is usually regarded as a powerful tool to probe the polarizable surface in vibrational energy levels [58]. It is reported that average Li⁺ concentration near the surface (less than 10 μm above the surface) of plated Li can be increased via strong Li⁺ affinity (e.g., Li–N) [25]. This can efficiently compensate lithium ions depletion, and mitigate the surface concentration difference, which leads to more uniform
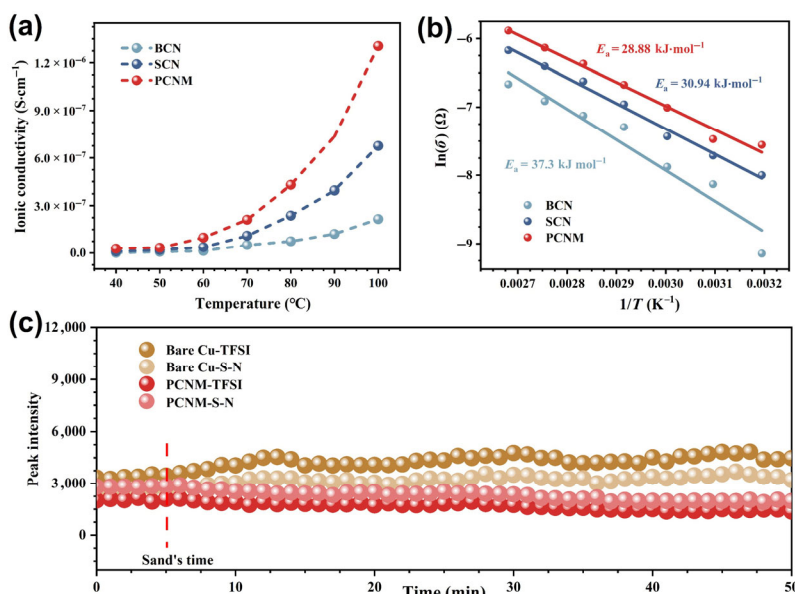
Figure 5 (a) Temperature dependent ionic conductivity plots and (b) corresponding activation energy of Cu@SCN, Cu@BCN, and Cu@PCNM. (c) Intensity evolution of Raman peaks of electrolytes in the cells using Cu foil coated with and without PCNM in charging process at 1 mA·cm^{-2}.

local current density distribution and Li-plating morphology. However, near interfacial (< 300 μm) Li$^+$ flux distribution/fluctuation which is related closely to the concentration gradient change of lithium ions upon strong Li$^+$ affinity still remains unknown. In addition, detecting concentration gradient change of the Li$^+$ flux is a more convenient way to investigate Li deposition behavior especially with some materials whose laser-induced signal will be shielded by excited fluorescence signal. Therefore, *in situ* Raman spectroscopy was conducted in a Li‖Cu cell to confirm the PCNM-regulated uniform Li$^+$ flux. The laser beam was set parallel to the Cu foil or Cu@PCNM and was focused near the interface of the electrodes (~ 300 μm above the surface) to detect the concentration gradient change of ion flux. The *operando* Raman spectra were measured during the Li plating process at the current density of 1 mA·cm^{-2} with an areal capacity of 1 mAh·cm^{-2}. Before the electrochemical plating process, the Raman spectrum of the electrolyte in Figs. S23(a) and S23(b) in the ESM shows featured bands at 741 and 941 cm^{-1}, corresponding to the S–N stretching in coordinated TFSI$^-$ and Li-coordinated solvent band, respectively, whose intensities can indirectly represent the Li$^+$ concentration [58, 59]. The peak intensity of S–N and TFSI$^-$ regarding bare Cu foil and Cu@PCNM is summarized in Fig. 5(e).

The peak intensity of TFSI$^-$ initially keeps at ~ 3,000 on both two electrodes. Bare Cu foil fluctuates from 3,200 to 4,900 with a range of ~ 1,700, while Cu@PCNM varies within only ~ 1,000 during charging. Meanwhile, the peak intensity of S–N keeps at ~ 2,300 at the beginning in both two electrodes, followed by fluctuating within a range of ~ 1,200 on bare Cu foil and ~ 700 on Cu@PCNM electrode, respectively. It should be noted that at the beginning of the plating (~ 5 min), initial stable nucleation and deposition play a dominant role in stabilizing the Li$^+$ flux near the interfacial area on bare Cu foil and Cu@PCNM before the formation of Li dendrites. Therefore, the peak intensities keep relatively stable during this period of time. It is referred that sphere-like Li seeds grow initially on Cu foil, followed by continuing preferential deposition on the Li seeds to form Li dendrites [50]. As the deposition proceeds, according to the dendrite growth model proposed by Chazalviel [60], the concentration of Li$^+$ in the vicinity (< 10 μm) of the negative electrode will drop to zero at Sand's time, leading to the apparent concentration gradient. Consequently, Li dendrite-

induced concentration gradient is reported to further intensify highly local disturbance of the Li$^+$ flux near the interfacial area of the negative electrode [25], leading to the formidable fluctuation of the Li$^+$ flux. Thus, bare Cu foil shows a large fluctuation range of ~ 1,700 and ~ 1,200 in TFSI$^-$ and S–N, respectively. In contrast, PCNM with N-rich Lewis-base sites and nano-channels can serve as a regulator to continually smooth the concentration of Li$^+$ flux [25] and ensure even ion flux in the vicinity of the electrochemical interface, resulting in dendrite-free deposition and weakening local disturbance of Li$^+$. As a result, smaller fluctuation of peak intensities (~ 1,000 and ~ 700 in TFSI$^-$ and S–N, respectively) due to the more stable Li$^+$ flux near the negative electrode is observed.

3.6 Electrochemical performances of full cells (coin and pouch cells)

To verify the practical performance of PCNM in full cells, long-term cycling and rate performance of full cells assembled with bare Li foil or Li foil@PCNM negative electrode (20 mAh·cm^{-2}) and LFP (~ 2 mAh·cm^{-2}) positive electrode were tested. Compared with bare Li foil, Li foil@PCNM composite negative electrode performs better rate capability as illustrated in Fig. 6(a). Especially at a high rate of 2 C, the cell using Li foil@PCNM still delivers a high specific capacity of ~ 125 mAh·g^{-1}, which is much higher than that of bare Li foil cell (~ 5 mAh·g^{-1}), revealing the stable discharge capacity at high rates owing to the PCNM-driven stable Li$^+$ flux. Figure 6(b) shows that the capacity retention of the full cell composed of bare Li foil undergoes a sharp drop to less than 10% after 100 cycles. In contrast, the full cell with Li foil@PCNM composite negative electrode exhibits a much higher capacity retention of ~ 97% after 100 cycles and ~ 80% after even more than 200 cycles. Compared with bare Li foil cell, Li foil@PCNM-based full cell exhibits lower voltage hysteresis at all different charge/discharge rates of 0.1, 0.2, 0.5, 1, and 2 C, and much more stable voltage hysteresis from the 5th to the 105th cycle (Figs. 6(c)–6(f)). The advantage of PCNM coating on Li negative electrodes in improving rate capability and cycling stability can be ascribed to the nano-channel induced uniform and stabilized Li$^+$ flux as well as confined growth of Li in PCNM, which leads to much smaller polarization and fast and
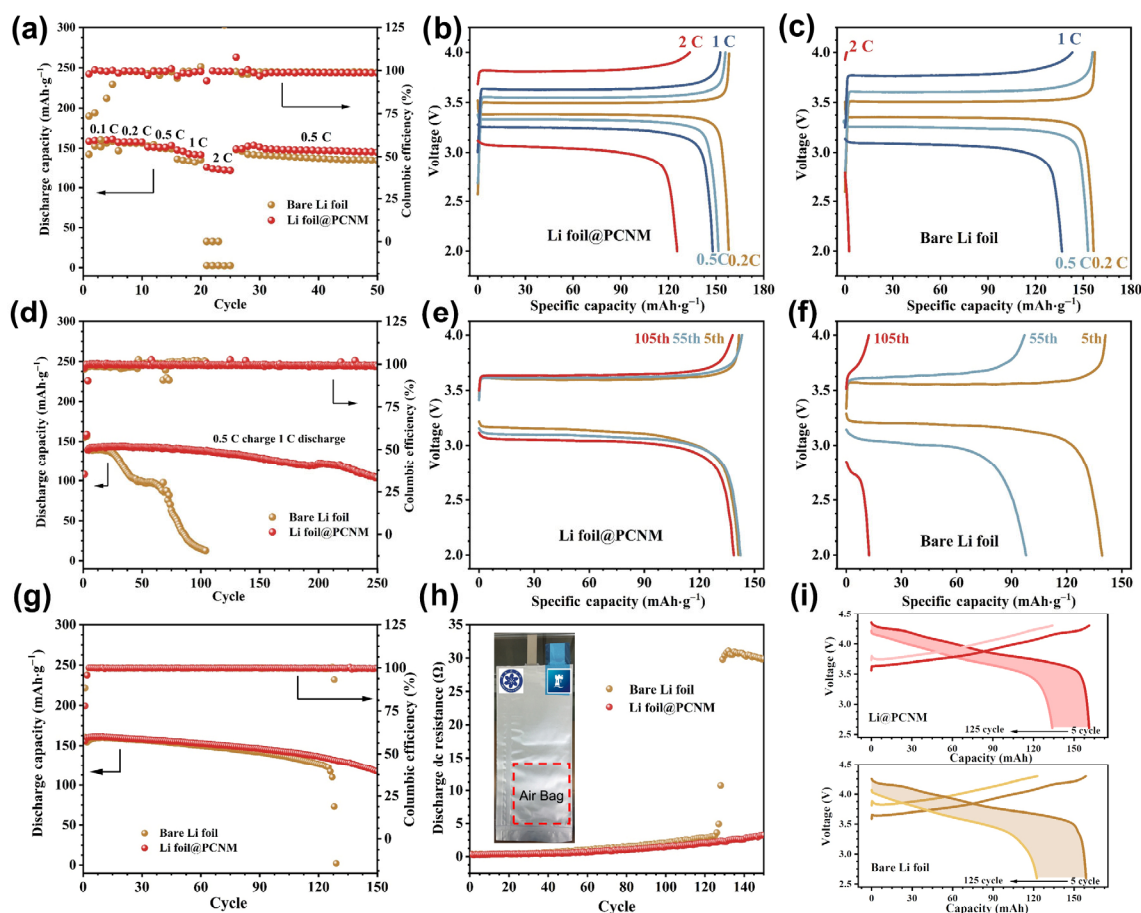
Figure 6 Performances of Li foil@PCNM in coin full cells and pouch cells. (a) Rate capability and (d) cycling performance of Li foil@PCNM electrodes and bare Li foil electrodes paired with high areal capacity LFP positive electrodes (~ 2 mAh·cm^{-2}). Voltage profiles of (b) Li foil@PCNM‖LFP full cell and (c) bare Li foil‖LFP full cell from 0.2 to 2 C. Voltage profiles of (e) Li foil@PCNM‖LFP full cell and (f) bare Li foil‖LFP full cell at the 5th, the 55th, and the 105th cycle. (g) Cycling performance and (h) *in situ* discharge internal resistance profiles of Li foil@PCNM electrodes and bare Li foil electrodes paired with high areal capacity NCM 811 positive electrodes (~ 3.75 mAh·cm^{-2}). (i) Voltage profiles of Li foil@PCNM‖NCM 811 pouch cell and bare Li foil‖NCM 811 pouch cells from the 5th to the 125th cycle.

uniform Li$^+$ transportation.

The compatibility and practical feasibility of Li foil@PCNM composite negative electrode (20 mAh·cm^{-2}) were further evaluated by pairing with NCM 811 positive electrode (~ 3.75 mAh·cm^{-2} on each side) in pouch-type full cells with a designed initial capacity of ~ 0.16 Ah and electrolyte mass of ~ 0.96 g. Li foil‖NCM 811 cells show apparent capacity and CE decay after 120 cycles at 0.2 C followed by a sudden drop, while Li foil@PCNM cells can maintain high capacity retention of ~ 73% after 150 cycles under the same condition. Figure 6(h) compares the internal resistances of pouch cells, which are *in situ* monitored to demonstrate the function of PCNM on lowering the electrochemical polarization of cells during cycling. In the first 20 cycles, the internal resistance of Li foil‖NCM 811 and Li foil@PCNM‖NCM 811 pouch cells show a similar rising trend (increasing from ~ 0.2 to ~ 0.4 Ω). Nevertheless, the internal resistance of Li foil‖NCM 811 cell suffers from a dramatic increase to ~ 30 Ω after 130 cycles, while that of Li foil@PCNM‖NCM 811 cells only gradually rises to ~ 2.7 Ω after more than 140 cycles. Smaller capacity decay (~ 25 mAh) can also be found in Li foil@PCNM‖NCM 811 cells than that in bare Li foil‖NCM 811 cells (almost doubled) from the 5th to the 125th cycle (Fig. 6(i)). More stable internal resistance and better cycling stability of Li foil@PCNM‖NCM 811 pouch cells than that of Li foil‖NCM 811 cells can be ascribed to the inhibition of "dead Li" and generation of more robust SEI by the PCNM coating.

4 Conclusions

In this work, we have firstly investigated the influence of morphology over g-C$_3$N$_4$ materials on Li deposition/dissolution behavior. Although a SCN layer can provide effective interaction with lithium ions during penetration of electrolyte, the 2D structure with lamellar connection was unable to accommodate Li growth and performed weak mechanical strength to absorb the increasing stress resulting from the growing Li dendrites. Though a large space was found within the BCN coating layer, efficient interaction between lithium ions and nitrogen atoms in g-C$_3$N$_4$ was limited due to the large pore size. In comparison, 3D porous framework of the PCNM coating layer containing both nano- and micro-pores was more favorable for physical regulation of Li deposition to rapidly absorb the stress change and guide Li growth, resulting in suppression of volume variation. Meanwhile, nanopores in PCNM can facilitate chemical interaction between lithium ions and N-containing functional groups, leading to homogenizing Li$^+$ distribution based on the Debye length law. The above physical-chemical synergic regulation strategy can promote dendrite-free Li plating. Resultantly, dense and stable deposition and highly reversible plating/stripping behavior over the PCNM-decorated Cu foil/Li foil were fully confirmed in three different coin cells, i.e., Cu@PCNM‖Li, Li foil@PCNM‖Li foil@PCNM, and Li foil@PCNM‖LFP, and a pouch cell, i.e., Li foil@PCNM‖NCM 811. This research provides novel insight in rational structure

design of lithiophilic materials for modification of Li negative electrodes toward stable and long-life lithium metal batteries.

Acknowledgements

References

[1] Lin, D. C.; Liu, Y. Y.; Cui, Y. Reviving the lithium metal anode for high-energy batteries. *Nat. Nanotechnol.* **2017**, *12*, 194–206.

[2] Lu, L. L.; Ge, J.; Yang, J. N.; Chen, S. M.; Yao, H. B.; Zhou, F.; Yu, S. H. Free-standing copper nanowire network current collector for improving lithium anode performance. *Nano Lett.* **2016**, *16*, 4431–4437.

[3] Lu, Z. Y.; Liang, Q. H.; Wang, B.; Tao, Y.; Zhao, Y. F.; Lv, W.; Liu, D. H.; Zhang, C.; Weng, Z.; Liang, J. C. et al. Graphitic carbon nitride induced micro-electric field for dendrite-free lithium metal anodes. *Adv. Energy Mater.* **2019**, *9*, 1803186.

[4] Cui, C. Y.; Yang, C. Y.; Eidson, N.; Chen, J.; Han, F. D.; Chen, L.; Luo, C.; Wang, P. F.; Fan, X. L.; Wang, C. S. A highly reversible, dendrite-free lithium metal anode enabled by a lithium-fluoride-enriched interphase. *Adv. Mater.* **2020**, *32*, 1906427.

[5] Zhang, X.; Yang, Y. A.; Zhou, Z. Towards practical lithium-metal anodes. *Chem. Soc. Rev.* **2020**, *49*, 3040–3071.

[6] Zheng, G. Y.; Lee, S. W.; Liang, Z.; Lee, H. W.; Yan, K.; Yao, H. B.; Wang, H. T.; Li, W. Y.; Chu, S.; Cui, Y. Interconnected hollow carbon nanospheres for stable lithium metal anodes. *Nat. Nanotechnol.* **2014**, *9*, 618–623.

[7] Cheng, M. R.; Su, H.; Xiong, P. X.; Zhao, X. X.; Xu, Y. H. Molten lithium-filled three-dimensional hollow carbon tube mats for stable lithium metal anodes. *ACS Appl. Energy Mater.* **2019**, *2*, 8303–8309.

[8] Lang, J. L.; Song, J. A.; Qi, L. H.; Luo, Y. Z.; Luo, X. Y.; Wu, H. Uniform lithium deposition induced by polyacrylonitrile submicron fiber array for stable lithium metal anode. *ACS Appl. Mater. Interfaces* **2017**, *9*, 10360–10365.

[9] Deng, W.; Liang, S. S.; Zhou, X. F.; Zhao, F.; Zhu, W. H.; Liu, Z. P. Depressing the irreversible reactions on a three-dimensional interface towards a high-areal capacity lithium metal anode. *J. Mater. Chem. A* **2019**, *7*, 6267–6274.

[10] He, Y.; Xu, H. W.; Shi, J. L.; Liu, P. Y.; Tian, Z. Q.; Dong, N.; Luo, K.; Zhou, X. F.; Liu, Z. P. Polydopamine coating layer modified current collector for dendrite-free Li metal anode. *Energy Storage Mater.* **2019**, *23*, 418–426.

[11] Liang, X.; Pang, Q.; Kochetkov, I. R.; Sempere, M. S.; Huang, H.; Sun, X. Q.; Nazar, L. F. A facile surface chemistry route to a stabilized lithium metal anode. *Nat. Energy* **2017**, *2*, 17119.

[12] Yang, C. P.; Liu, B. Y.; Jiang, F.; Zhang, Y.; Xie, H.; Hitz, E.; Hu, L. B. Garnet/polymer hybrid ion-conducting protective layer for stable lithium metal anode. *Nano Res.* **2017**, *10*, 4256–4265.

[13] Wu, Q. P.; Yao, Z. G.; Du, A. C.; Wu, H.; Huang, M. S.; Xu, J.; Cao, F. H.; Li, C. L. Oxygen-defect-rich coating with nanoporous texture as both anode host and artificial SEI for dendrite-mitigated lithium–metal batteries. *J. Mater. Chem. A* **2021**, *9*, 5606–5618.

[14] Li, T.; Shi, P.; Zhang, R.; Liu, H.; Cheng, X. B.; Zhang, Q. Dendrite-free sandwiched ultrathin lithium metal anode with even lithium plating and stripping behavior. *Nano Res.* **2019**, *12*, 2224–2229.

[15] Sun, H.; Zhu, G. Z.; Zhu, Y. M.; Lin, M. C.; Chen, H.; Li, Y. Y.; Hung, W. H.; Zhou, B.; Wang, X.; Bai, Y. X. et al. High-safety and high-energy-density lithium metal batteries in a novel ionic-liquid electrolyte. *Adv. Mater.* **2020**, *32*, 2001741.

[16] Shi, P. C.; Liu, F. F.; Feng, Y. Z.; Zhou, J. F.; Rui, X. H.; Yu, Y. The synergetic effect of lithium bisoxalatodifluorophosphate and fluoroethylene carbonate on dendrite suppression for fast charging lithium metal batteries. *Small* **2020**, *16*, 2001989.

[17] Zhang, W. D.; Wu, Q.; Huang, J. X.; Fan, L.; Shen, Z. Y.; He, Y.; Feng, Q.; Zhu, G. N.; Lu, Y. Y. Colossal granular lithium deposits enabled by the grain-coarsening effect for high-efficiency lithium metal full batteries. *Adv. Mater.* **2020**, *32*, 2001740.

[18] Yan, K.; Lu, Z. D.; Lee, H. W.; Xiong, F.; Hsu, P. C.; Li, Y. Z.; Zhao, J.; Chu, S.; Cui, Y. Selective deposition and stable encapsulation of lithium through heterogeneous seeded growth. *Nat. Energy* **2016**, *1*, 16010.

[19] Yao, Y.; Xu, R.; Chen, M. L.; Cheng, X. L.; Zeng, S. F.; Li, D. J.; Zhou, X. F.; Wu, X. J.; Yu, Y. Encapsulation of SeS₂ into nitrogen-doped free-standing carbon nanofiber film enabling long cycle life and high energy density K-SeS₂ battery. *ACS Nano* **2019**, *13*, 4695–4704.

[20] Yang, G. J.; Li, Y. J.; Tong, Y. X.; Qiu, J. L.; Liu, S.; Zhang, S. M.; Guan, Z. R.; Xu, B.; Wang, Z. X.; Chen, L. Q. Lithium plating and stripping on carbon nanotube sponge. *Nano Lett.* **2019**, *19*, 494–499.

[21] Fan, L.; Zhuang, H. L.; Zhang, W. D.; Fu, Y.; Liao, Z. H.; Lu, Y. Y. Stable lithium electrodeposition at ultra-high current densities enabled by 3D PMF/Li composite anode. *Adv. Energy Mater.* **2018**, *8*, 1703360.

[22] Luan, X. Y.; Wang, C. G.; Wang, C. S.; Gu, X.; Yang, J.; Qian, Y. T. Stable lithium deposition enabled by an acid-treated g-C₃N₄ interface layer for a lithium metal anode. *ACS Appl. Mater. Interfaces* **2020**, *12*, 11265–11272.

[23] Wang, X. S.; Pan, Z. H.; Wu, Y.; Ding, X. Y.; Hong, X. J.; Xu, G. G.; Liu, M. N.; Zhang, Y. G.; Li, W. S. Infiltrating lithium into carbon cloth decorated with zinc oxide arrays for dendrite-free lithium metal anode. *Nano Res.* **2019**, *12*, 525–529.

[24] Zhang, Y.; Liu, B. Y.; Hitz, E.; Luo, W.; Yao, Y. G.; Li, Y. J.; Dai, J. Q.; Chen, C. J.; Wang, Y. B.; Yang, C. P. et al. A carbon-based 3D current collector with surface protection for Li metal anode. *Nano Res.* **2017**, *10*, 1356–1365.

[25] Li, G. X.; Liu, Z.; Huang, Q. Q.; Gao, Y.; Regula, M.; Wang, D. W.; Chen, L. Q.; Wang, D. H. Stable metal battery anodes enabled by polyethylenimine sponge hosts by way of electrokinetic effects. *Nat. Energy* **2018**, *3*, 1076–1083.

[26] Ni, S. Y.; Tan, S. S.; An, Q. Y.; Mai, L. Q. Three dimensional porous frameworks for lithium dendrite suppression. *J. Energy Chem.* **2020**, *44*, 73–89.

[27] Wu, H. L.; Zhang, Y. B.; Deng, Y. Q.; Huang, Z. J.; Zhang, C.; He, Y. B.; Lv, W.; Yang, Q. H. A lightweight carbon nanofiber-based 3D structured matrix with high nitrogen-doping level for lithium metal anodes. *Sci. China Mater.* **2019**, *62*, 87–94.

[28] Zhang, R.; Chen, X. R.; Chen, X.; Cheng, X. B.; Zhang, X. Q.; Yan, C.; Zhang, Q. Lithiophilic sites in doped graphene guide uniform lithium nucleation for dendrite-free lithium metal anodes. *Angew. Chem., Int. Ed.* **2017**, *56*, 7764–7768.

[29] Guo, Y. P.; Niu, P.; Liu, Y. Y.; Ouyang, Y.; Li, D.; Zhai, T. Y.; Li, H. Q.; Cui, Y. An autotransferable g-C$_3$N$_4$ Li$^+$-modulating layer toward stable lithium anodes. *Adv. Mater.* **2019**, *31*, 1900342.

[30] Huang, Y.; Chen, B.; Duan, J.; Yang, F.; Wang, T. R.; Wang, Z. F.; Yang, W. J.; Hu, C. C.; Luo, W.; Huang, Y. H. Graphitic carbon nitride (g-C$_3$N$_4$): An interface enabler for solid-state lithium metal batteries. *Angew. Chem., Int. Ed.* **2020**, *59*, 3699–3704.

[31] Yang, Q. F.; Cui, M. N.; Hu, J. L.; Chu, F. L.; Zheng, Y. J.; Liu, J. J.; Li, C. L. Ultrathin defective C-N coating to enable nanostructured Li plating for Li metal batteries. *ACS Nano* **2020**, *14*, 1866–1878.

[32] Xu, Y.; Li, T.; Wang, L. P.; Kang, Y. J. Interlayered dendrite-free lithium plating for high-performance lithium-metal batteries. *Adv. Mater.* **2019**, *31*, 1901662.

[33] Guo, Y. P.; Wei, Y. Q.; Li, H. Q.; Zhai, T. Y. Layer structured materials for advanced energy storage and conversion. *Small* **2017**, *13*, 1701649.

[34] Pennathur, S.; Santiago, J. G. Electrokinetic transport in nanochannels. 2. Experiments. *Anal. Chem.* **2005**, *77*, 6782–6789.

[35] Hu, J. L.; Tian, J.; Li, C. L. Nanostructured carbon nitride polymer-reinforced electrolyte to enable dendrite-suppressed lithium metal batteries. *ACS Appl. Mater. Interfaces* **2017**, *9*, 11615–11625.

[36] Hu, J. L.; Chen, K. Y.; Yao, Z. G.; Li, C. L. Unlocking solid-state conversion batteries reinforced by hierarchical microsphere stacked polymer electrolyte. *Sci. Bull.* **2021**, *66*, 694–707.

[37] Liu, G. Q.; Xue, M. W.; Liu, Q. P.; Yang, H.; Zhou, Y. M. Facile synthesis of C-doped hollow spherical g-C$_3$N$_4$ from supramolecular self-assembly for enhanced photoredox water splitting. *Int. J. Hyd. Energy* **2019**, *44*, 25671–25679.

[38] Kuang, P. Y.; Su, Y. Z.; Chen, G. F.; Luo, Z.; Xing, S. Y.; Li, N.; Liu, Z. Q. g-C$_3$N$_4$ decorated ZnO nanorod arrays for enhanced photoelectrocatalytic performance. *Appl. Surf. Sci.* **2015**, *358*, 296–303.

[39] Liu, Y. J.; Liu, H. X.; Zhou, H. M.; Li, T. D.; Zhang, L. N. A Z-scheme mechanism of N-ZnO/g-C$_3$N$_4$ for enhanced H$_2$ evolution and photocatalytic degradation. *Appl. Surf. Sci.* **2019**, *466*, 133–140.

[40] Guo, Q.; Wan, Y. L.; Hu, B. B.; Wang, X. T. Carbon-nitride-based core–shell nanomaterials: Synthesis and applications. *J. Mater. Sci. Mater. Electron.* **2018**, *29*, 20280–20301.

[41] Uma, R.; Ravichandran, K.; Sriram, S.; Sakthivel, B. Cost-effective fabrication of ZnO/g-C$_3$N$_4$ composite thin films for enhanced photocatalytic activity against three different dyes (MB, MG and RhB). *Mater. Chem. Phys.* **2017**, *201*, 147–155.

[42] Li, L.; Sun, S. Q.; Wang, Y. X.; Wang, C. Y. Facile synthesis of ZnO/g-C$_3$N$_4$ composites with honeycomb-like structure by H$_2$ bubble templates and their enhanced visible light photocatalytic performance. *J. Photochem. Photobiol. A Chem.* **2018**, *355*, 16–24.

[43] Chu, M. N.; Hu, K.; Wang, J. S.; Liu, Y. D.; Ali, S.; Qin, C. L.; Jing, L. Q. Synthesis of g-C$_3$N$_4$-based photocatalysts with recyclable feature for efficient 2,4-dichlorophenol degradation and mechanisms. *Appl. Catal. B Environ.* **2019**, *243*, 57–65.

[44] Li, C.; Zhao, W.; Wang, A. J.; Zhu, W. H.; Shang, D. H. Multifunctional carbon nitride nano-homojunction decorated g-C$_3$N$_4$ nanocomposites for optoelectronic performances. *Appl. Surf. Sci.* **2019**, *467–468*, 1140–1147.

[45] Guo, Q.; Fu, L. M.; Yan, T.; Tian, W.; Ma, D. F.; Li, J. M.; Jiang, Y. N.; Wang, X. T. Improved photocatalytic activity of porous ZnO nanosheets by thermal deposition graphene-like g-C$_3$N$_4$ for CO$_2$ reduction with H$_2$O vapor. *Appl. Surf. Sci.* **2020**, *509*, 144773.

[46] Qi, K. Z.; Xie, Y. B.; Wang, R. D.; Liu, S. Y.; Zhao, Z. Electroless plating Ni-P cocatalyst decorated g-C$_3$N$_4$ with enhanced photocatalytic water splitting for H$_2$ generation. *Appl. Surf. Sci.* **2019**, *466*, 847–853.

[47] Liu, N.; Lu, N.; Su, Y.; Wang, P.; Quan, X. Fabrication of g-C$_3$N$_4$/Ti$_3$C$_2$ composite and its visible-light photocatalytic capability for ciprofloxacin degradation. *Sep. Purif. Technol.* **2019**, *211*, 782–789.

[48] Yu, W. L.; Xu, D. F.; Peng, T. Y. Enhanced photocatalytic activity of g-C$_3$N$_4$ for selective CO$_2$ reduction to CH$_3$OH via facile coupling of ZnO: A direct Z-scheme mechanism. *J. Mater. Chem. A* **2015**, *3*, 19936–19947.

[49] Ryou, M. H.; Lee, D. J.; Lee, J. N.; Lee, Y. M.; Park, J. K.; Choi, J. W. Excellent cycle life of lithium-metal anodes in lithium-ion batteries with mussel-inspired polydopamine-coated separators. *Adv. Energy Mater.* **2012**, *2*, 645–650.

[50] Meng, Q. Q.; Deng, B.; Zhang, H. M.; Wang, B. Y.; Zhang, W. F.; Wen, Y. H.; Ming, H.; Zhu, X. Y.; Guan, Y. P.; Xiang, Y. et al. Heterogeneous nucleation and growth of electrodeposited lithium metal on the basal plane of single-layer graphene. *Energy Storage Mater.* **2019**, *16*, 419–425.

[51] Alpen, U. V. Li$_3$N: A promising Li ionic conductor. *J. Solid State Chem.* **1979**, *29*, 379–392.

[52] Ye, S. F.; Wang, L. F.; Liu, F. F.; Shi, P. C.; Wang, H. Y.; Wu, X. J.; Yu, Y. g-C$_3$N$_4$ derivative artificial organic/inorganic composite solid electrolyte interphase layer for stable lithium metal anode. *Adv. Energy Mater.* **2020**, *10*, 2002647.

[53] Liu, S. F.; Ji, X.; Piao, N.; Chen, J.; Eidson, N.; Xu, J. J.; Wang, P. F.; Chen, L.; Zhang, J. X.; Deng, T. et al. An inorganic-rich solid electrolyte interphase for advanced lithium-metal batteries in carbonate electrolytes. *Angew. Chem., Int. Ed.* **2021**, *60*, 3661.

[54] Pu, J.; Li, J. C.; Zhang, K.; Zhang, T.; Li, C. W.; Ma, H. X.; Zhu, J.; Braun, P. V.; Lu, J.; Zhang, H. G. Conductivity and lithiophilicity gradients guide lithium deposition to mitigate short circuits. *Nat. Commun.* **2019**, *10*, 1896.

[55] Dong, N.; Yang, G. H.; Luo, H.; Xu, H. W.; Xia, Y. G.; Liu, Z. P. A LiPO$_2$F$_2$/LiFSI dual-salt electrolyte enabled stable cycling of lithium metal batteries. *J. Power Sources* **2018**, *400*, 449–456.

[56] Jeon, Y.; Kang, S. J.; Joo, S. H.; Cho, M.; Park, S. O.; Liu, N.; Kwak, S. K.; Lee, H. W.; Song, H. K. Pyridinic-to-graphitic conformational change of nitrogen in graphitic carbon nitride by lithium coordination during lithium plating. *Energy Storage Mater.* **2020**, *31*, 505–514.

[57] Whiteley, J. M.; Hafner, S.; Han, S. S.; Kim, S. C.; Oh, K. H.; Lee, S. H. FeS$_2$-imbedded mixed conducting matrix as a solid battery cathode. *Adv. Energy Mater.* **2016**, *6*, 1600495.

[58] Hu, Y.; Chen, W.; Lei, T. Y.; Jiao, Y.; Wang, H. B.; Wang, X. P.; Rao, G. F.; Wang, X. F.; Chen, B.; Xiong, J. Graphene quantum dots as the nucleation sites and interfacial regulator to suppress lithium dendrites for high-loading lithium-sulfur battery. *Nano Energy* **2020**, *68*, 104373.

[59] Cheng, Q.; Wei, L.; Liu, Z.; Ni, N.; Sang, Z.; Zhu, B.; Xu, W. H.; Chen, M. J.; Miao, Y. P.; Chen, L. Q. et al. Operando and three-dimensional visualization of anion depletion and lithium growth by stimulated Raman scattering microscopy. *Nat. Commun.* **2018**, *9*, 2942.

[60] Chazalviel, J. N. Electrochemical aspects of the generation of ramified metallic electrodeposits. *Phys. Rev. A* **1990**, *42*, 7355–7367.